Two-magnon scattering in permalloy thin films due to rippled substrates

M. Körner,[1,2,*] K. Lenz,[1] R. A. Gallardo,[3] M. Fritzsche,[1,2] A. Mücklich,[1] S. Facsko,[1] J. Lindner,[1] P. Landeros,[3] and J. Fassbender[1,2]

[1]*Institute of Ion Beam Physics and Materials Research, Helmholtz-Zentrum Dresden-Rossendorf e.V., Bautzner Landstr. 400, 01328 Dresden, Germany*

[2]*Institute for Physics of Solids, TU Dresden, Zellescher Weg 16, 01069 Dresden, Germany*

[3]*Departamento de Física, Universidad Técnica Federico Santa María, Av. España 1680, Valparaíso, Chile*

(Received 20 March 2013; revised manuscript received 2 July 2013; published 9 August 2013)

We report on the influence of correlated substrate roughness on the two-magnon scattering in 30 nm $Ni_{81}Fe_{19}$ thin films. Using ion beam erosion, periodically modulated substrates (ripple) were produced with wavelengths between 20 and 432 nm. This surface corrugation is adopted by magnetic layers grown on top yielding dipolar stray fields if magnetization and ripple ridges are aligned perpendicular to each other. In case of $\lambda \geqslant 222$ nm, the evolving periodic field pattern triggers two-magnon scattering, which depends strongly on the direction of magnetization with respect to the ripple pattern. In-plane broadband ferromagnetic resonance reveals prominent peaks in the frequency-dependent linewidth measured perpendicularly to the ripple ridges. These peaks can be switched off if the magnetization is aligned along the ripple ridges. Our results are compared to predictions obtained from recent theory on spin waves in periodically perturbed films.

DOI: 10.1103/PhysRevB.88.054405 PACS number(s): 76.50.+g, 75.78.−n, 75.30.Ds, 75.78.Cd

I. INTRODUCTION

Magnetic relaxation processes have gained a broad interest over the past decades since a detailed understanding of the underlying physical mechanisms offers the possibility to specifically tailor magnetization dynamics in ferromagnetic thin films.[1,2] This is of crucial importance when pursuing new devices concepts, e.g., in spintronics or spin-torque applications, where the control of magnetization damping is essential for functionality.[3–6] The Gilbert damping is studied since decades.[7–12] As it is mainly isotropic in 3*d* ferromagnets[13] it does not offer much possibilities of influencing the magnetic relaxation without changing intrinsic material properties. In contrast, extrinsic relaxation contributions can be induced artificially, e.g., by defects or misfit dislocations due to Pd capping layers.[14] Hence this approach offers the possibility to tailor the relaxation rate to some extent. Among all extrinsic relaxation mechanisms, two-magnon scattering (TMS) is the most prominent contribution. It is known for bulk materials since the late 1950s[15,16] and was confirmed in thin films a decade later.[17] A standard tool to study both relaxation paths is given by ferromagnetic resonance (FMR). In FMR, the linewidth is a direct measure of the relaxation allowing to disentangle the contributions. TMS contributions introduce nonlinearities by scattering energy from the excited uniform mode ($k = 0$) into degenerate spin wave states ($k \neq 0$). This is activated by scattering centers, e.g., randomly distributed surface defects.[18] Besides that, defects in magnetic films may induce inhomogeneous broadening of the linewidth.[19,20] As a consequence of TMS linewidth broadening and/or a shifted resonance field of the $k = 0$ spin wave mode were observed in $Ni_{50}Fe_{50}$ thin films,[21] Fe/V multilayers,[22,23] Fe_3Si,[24] or Fe[14] thin films.

Approaches to specifically influence the frequency-dependent linewidth by artificially modifying the sample's layout were for instance realized by coupling $Ni_{90}Fe_{10}$ to a synthetic antiferromagnet,[25] altering a seed layer beneath a $Fe_{65}Co_{35}$ layer,[26] or by changing the samples structure by making grooves[27,28] into the substrate. Especially, in the latter case, the frequency-dependent linewidth increases non-monotonously in frequency when recorded perpendicularly to the groove ridges. Recently, Barsukov *et al.* have used patterned periodical stripe defects on top of thin permalloy ($Ni_{81}Fe_{19} \equiv$ Py) films that showed a similar behavior strongly deviating from the linear Gilbert damping behavior usually expected in the frequency dependence.[29] In fact, distinct peaks appeared in the linewidth whose frequency positions are determined by the defect width, its periodicity, and the material properties when measuring perpendicularly to the stripe defects. This is understood in the framework of a theory on spin waves in periodically perturbed films, presented by Landeros and Mills very recently assuming stripelike defects on top of a magnetic thin film.[30] Hence a variety of possibilities exists to tailor magnetization dynamics by externally altering the sample properties. However, due to the variety of contributing relaxation processes the FMR linewidth may not automatically be interpreted as magnetization damping, which is considered as dissipation of energy from the spin system to the lattice. Especially if TMS is taken into account, the excited uniform mode ($k = 0$) undergoes a relaxation process distributing the energy *within* the spin system to higher order spin waves with $k \neq 0$ that in turn may scatter back to the uniform mode. Hence also the damping of $k \neq 0$ modes needs to be taken into account.

The focus of this paper lies on the influence of the substrate morphology exhibiting a correlated, anisotropic surface modulation (obtained by ion-induced nanopatterning) on the extrinsic TMS relaxation process. In comparison to lithographic approaches combined with ion irradiation,[29] rippled samples are much easier in preparation and offer a continuous surface modulation on a large sample area, while leaving the magnetic material unaffected.[31,32] After reviewing the underlying perturbation theory of Landeros and Mills in

 ©2013 American Physical Society

Sec. II, details on sample structure and its preparation are presented in Sec. III and discussed in Sec. IV. Finally, our findings are summarized in Sec. V.

II. PERTURBATION THEORY: A REVIEW

In the following, the basic assumptions and findings of the perturbation theory presented by Landeros and Mills are shortly reviewed. For further details, the reader is kindly referred to Ref. 30 as well as Ref. 18. The latter reference contains the underlying response theory of Arias and Mills for in-plane magnetized ultrathin films exhibiting TMS, which in turn also was extended to the out-of-plane case.[33,34] Here, we will restrict all considerations to the in-plane case only.

The spin wave dispersion relation of an in-plane magnetized $d = 30$ nm thin Py film can be expressed in terms of the stiffness fields[18,35] $H_{||}$, H_z by

$$\omega(k) = \gamma\sqrt{H_{||}(k)\,H_z(k)}, \tag{1}$$

where k denotes the absolute value of the in-plane spin wave propagation vector with frequency $f = \omega(k)/(2\pi)$ and $\gamma = g\mu_B/\hbar$ is the absolute value of the gyromagnetic ratio containing the g factor. Note that in the present case, the coordinate system is fixed to the sample geometry as it is commonly used in experiments. In contrast, in the theory of Landeros *et al.*,[33] the stiffness fields rotate with the magnetization as it is required for the Hamiltonian, so $H_{||}(k)$ labels the stiffness field in the plane but perpendicular to the magnetization. The stiffness fields include the applied magnetic field H, the exchange stiffness $D = 2A/M_s$, saturation magnetization M_s, and an in-plane uniaxial magnetic anisotropy (UMA) constant $K_{2||}$:[33–35]

$$H_{||}(k) = \mu_0 H\cos(\varphi-\varphi_H) + \frac{2K_{2||}}{M_s}\cos 2(\varphi-\varphi_u) + \mu_0 M_s\left[1-\frac{1-\exp(-kd)}{kd}\right]\sin^2\varphi_k + Dk^2 \tag{2}$$

and

$$H_z(k) = \mu_0 H\cos(\varphi-\varphi_H) + \frac{2K_{2||}}{M_s}\cos^2(\varphi-\varphi_u) - \mu_0 M_s\left[1-\frac{1-\exp(-kd)}{kd}\right] + Dk^2 + \mu_0 M_{\text{eff}}. \tag{3}$$

Here, $\mu_0 M_{\text{eff}} = \mu_0 M_s - 2K_{2\perp}/M_s$ is the effective magnetization containing the out-of-plane uniaxial anisotropy $K_{2\perp}$. The equilibrium angle of M (φ), the field direction (φ_H), and the in-plane UMA direction (φ_u) are measured from the x direction (see Fig. 1). φ_k is the angle between magnetization and spin wave propagation direction.

For parallel alignment or small values of φ_k, the spin wave dispersion relation becomes degenerate in energy. If the magnetization is tipped out of the plane, the degenerate magnon state vanishes if the angle between the magnetization and the plane is larger than 45°.[33] The case of degenerate states is shown in Fig. 2(a) for $\mu_0 M_s = 1$ T, $d = 30$ nm, $D = 24$ T nm^2, $g = 2.11$, and vanishing anisotropy constants K_i, while using different external field values. In order to scatter energy from the excited $k = 0$ to the degenerate state, a periodic scattering potential is mandatory that triggers the process and fulfills momentum conservation. Assuming this potential has the periodicity $a_0 = 250$ nm in real space, its reciprocal lattice vector is given by $g_0 = 2\pi/a_0$. Integer multiples $g_m = mg_0$ ($m > 0$) of g_0 are displayed in Fig. 2(a) by dashed lines, whereby the field values in the dispersion relation are chosen in a way to match the degenerate states and reciprocal vectors. If this requirement is fulfilled, TMS may occur, while field values in between will not match the periodicity and, thus, do not contribute to the scattering substantially. Hence, for the frequency-dependent linewidth mainly distinct field values, and so frequencies, will cause

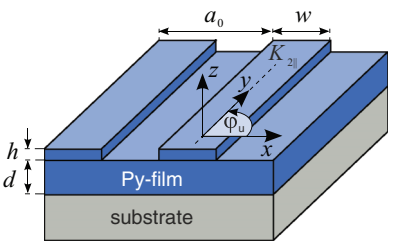

FIG. 1. (Color online) Geometry used in the perturbation model. Like φ_u the angles φ, φ_H of magnetization **M** and external field **H** (not shown) are lying in the xy plane and are measured from x.

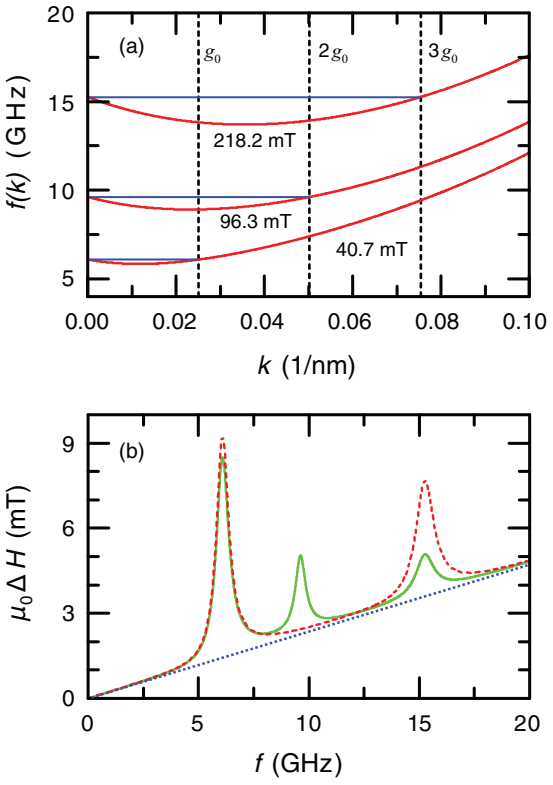

FIG. 2. (Color online) (a) Spin wave dispersion of a $d = 30$ nm thin Py film for different external fields. Dashed lines mark multiples of $g_0 = 2\pi/a_0$ with $a_0 = 250$ nm. (b) Modeled linewidth if a perturbation of $h = 3$ nm is assumed as well as a Gilbert damping of $\alpha = 0.007$. Defect widths are 100 (green, solid), 125 (red, dashed), and 250 (blue, dotted) nm.

TMS. Therefore distinct peaks are visible in Fig. 2(b), centered at the degenerate frequencies.

In order to induce a periodic defect structure in a thin magnetic film a stripelike pattern was assumed in Ref. 30 on the film's top with a periodicity of a_0 and a width of w, as depicted in Fig. 1. This steplike surface perturbation can be described by the Fourier series

$$h^{\text{step}}(x) = \frac{h}{\pi} \sum_{m=-\infty}^{\infty} \frac{\sin(m\pi w/a_0)}{m} \exp(\mathrm{i}mg_0 x), \qquad (4)$$

where h is the step height. Since the stripes are formed by magnetic material dipolar stray fields evolve at the step faces that penetrate the ferromagnetic layer beneath forming the periodic scattering potential. The evolving dipolar stray field and its comparison to the actual case of rippled samples will be discussed in detail in the following section.

Note that the theory presented in Ref. 30 considers stripelike defect structures where the associated magnetic charge distribution is 1D, i.e., it does not depend on the coordinate normal to the nominal film. Hence the charges reside in well defined positions $x = m\,a_0$. If one considers just the first Fourier contribution ($m = \pm 1$) of function (4) to obtain a sinusoidal profile quite similar to the ripples, this would violate the assumption made for the periodic *one-dimensional* charge distribution.

Finally, from the stray field the scattering matrix can be calculated, which enters the response function of the magnetic film and allows to calculate the half-width half-maximum linewidth in presence of the perturbations:

$$\Delta H = \frac{\Lambda(0) + \Gamma^{\mathrm{I}}(\omega)}{\gamma^2 [H_{||}(0) + H_z(0)]}. \qquad (5)$$

$\Lambda(k)$ is a wave vector dependent function linear in frequency containing the stiffness fields and intrinsic damping constant α, while $\Gamma^{\mathrm{I}}(\omega)$ is the imaginary part of a frequency-dependent function containing information about the perturbation and being responsible for the TMS response of the film. For both functions, the explicit form may be found in Ref. 30. As an example Fig. 2(b) depicts the evolving frequency-dependent linewidth of a perturbed film for different choices of the defect width w using the same parameters as in Fig. 2(a). In addition, $\alpha = 0.007$ and $h = 3$ nm were chosen. As shown in the graph, the linewidth shows in the depicted range up to three distinct peaks that are influenced by the ratio between defect width w and periodicity a_0.

In the case that defect width and periodicity are equal, the linewidth reveals only a linear increase having no peak, which is understood since this case approximates the planar limit having no perturbation at all. Focusing on the case $w = 100$ nm three peaks are visible that correspond to the degenerate state g_0 and its multiples [see Fig. 2(a)]. As shown by the $w = 125$ nm example, the peaks are not always visible and vary in height. The reason is the ratio of w and a_0 causing Fourier components in Eq. (4) to vanish if $m\pi w/a_0$ becomes a multiple of π. With respect to the peak height, h has the strongest influence (not shown), since it quantifies the strength of the scattering potential. This is a consequence of the magnetic charges of the defects, which naturally increase with h. For a fixed a_0 the relative peak position is given by $\omega(k = 0) = \omega(k = mg_0)$ and depends on the film's thickness and material parameters D, M_s, and anisotropy fields K_i. Furthermore, the stiffness field $H_{||}$ [see Eq. (2)] includes the spin wave propagation angle φ_k, which will change with the external field and additionally shifts the peak position, as will be shown later. It should be noted that the TMS mechanisms may cause a shift and splitting of the observed FMR mode as Γ^{I} is strongly frequency dependent. This is predicted by the theory for the response function but explicitly neglected in the calculation of the linewidth given in Eq. (5), which thus is only valid for small enough perturbations. As it will be seen later this is the case for rippled films.

In the experimental section following below, the surface corrugation caused by ripples will be compared to the stripe case assumed in the perturbation theory with respect to the evolving dipolar fields. Furthermore, the influence of the measured linewidth and the applicability of the model will be discussed.

III. EXPERIMENTAL DETAILS

In order to investigate the influence of the substrate morphology onto dynamic magnetic properties two kinds of Si(100) substrates were used: (i) planar samples for reference purposes and (ii) rippled substrates with a well defined surface modulation of periodicity λ. The rippled substrates were produced by ion beam erosion using Ar^+ or Xe^+ ions under an angle of 65°–67° with respect to the sample's normal, where the primary ion energy determines the wavelength of the modulation.[36] Details of the preparation process are reported in Ref. 37. Due to sample transfer under ambient conditions both samples exhibit an amorphous surface layer of natural oxide (SiO_2). In case of the rippled samples, the necessary sputtering process during the sample preparation causes a much thicker (dependent on ion energy) amorphous layer compared to naturally oxidized (usually up to 2 nm in thickness) substrates.

After substrate preparation, atomic force microscopy (AFM) was performed to determine the morphology and ensure substrate quality. Subsequently, the templates were sonicated in an isopropanol bath, inserted into a molecular beam epitaxy system, and annealed to 200 °C. The 30 nm Py film was deposited at a base pressure of less than 10^{-10} mbar using a rate below 0.2 Å/s. To prevent the sample from further oxidation, a 3 nm Cr cap was grown. After sample preparation, a second AFM measurement was performed in order to check potential changes in the surface morphology. Image processing was done using WSXM[38] and GWYDDION[39] software. To access the film's structure across the Py thickness transmission electron microscopy (TEM) was applied. Therefore lamellae (thickness below 100 nm) were cut from the films using a focused ion beam (FIB) method. The TEM cross-section images were used to extract the layer's shape, which allowed for calculating the magnetic configuration and the evolving dipolar stray fields using the micromagnetic simulation package OOMMF.[40] Finally, magnetic characterization was performed by means of vector network analyzer ferromagnetic resonance (VNA-FMR). An Agilent E8364B two-port VNA was used to generate microwaves with frequencies from 10 MHz up to 50 GHz with an amplified power of up to 500 mW coupled

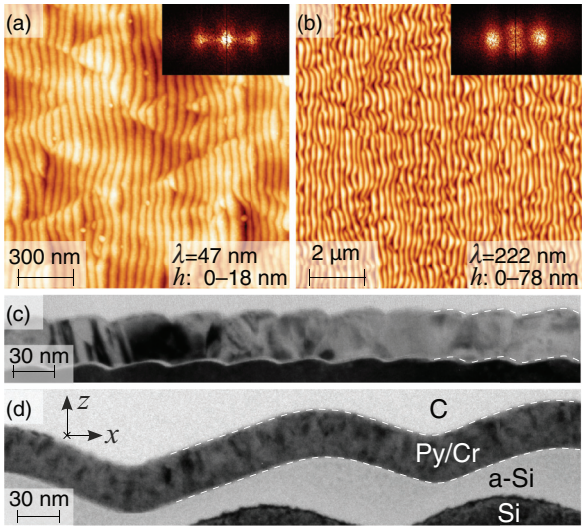

FIG. 3. (Color online) (a) and (b) Sample characterization using AFM (height scale labeled by h, insets show the 2D FFT) prior to layer deposition. (c) and (d) TEM images taken after deposition. In (a) and (c), images are shown for ripples with $\lambda = 47$ nm and in (b) and (d) for $\lambda = 222$ nm.

into a coplanar waveguide (CPW). The CPW's width was 80 μm and the samples were placed face-down on the CPW. By sweeping an external magnetic field, applied in-plane and perpendicularly to the microwave field, the FMR signal was recorded using the complex microwave scattering parameter S_{21}, i.e., the transmission of microwaves emitted from port one and received on port two of the VNA.

IV. RESULTS AND DISCUSSION

As already mentioned, in a first step the rippled substrates were characterized after ion beam erosion with respect to their surface morphology using AFM. Two corresponding images are shown in Figs. 3(a) and 3(b), respectively. The wavelength of the surface modulation can be extracted by using the 2D fast Fourier transformation (FFT), which is depicted by the insets. The FFTs clearly underline the anisotropy of the surface by showing two satellite peaks. From the distance between both peaks, the ripple wavelength λ can be derived. Additionally, the root mean square (rms) roughness was calculated from these images. A summary of the samples is given in Table I. One observes an increase in rms roughness and ripple peak-to-peak amplitude δ for increasing wavelength, where the only exception is the sample with the highest wavelength of $\lambda = 432$ nm. In this case, a superstructure started to appear caused by nonlinear effects during ion beam erosion.[41] After material growth, the rms value usually increases slightly, whereas the ripple wavelength stays constant. Further studies on this may be found in Ref. 32. Due to the high ripple peak-to-peak amplitudes in case of high wavelengths—around the film's thickness and beyond—the question arises whether the assumption of perturbation is still valid and, additionally, how dipolar fields are distributed in comparison to the assumed stripe case of the model.[30]

To investigate the material growth and to answer whether rippled films can be viewed as being perturbed, TEM

TABLE I. Structural parameters (periodicity λ, rms roughness, and peak-to-peak height δ) as well as magnetic parameters (exchange stiffness D, inhomogeneous linewidth contribution ΔH_{pp}^{inh}, and damping constant α) of the samples. Along the easy axes α equals the hard axis values except for $\lambda = 222$ nm, where $\alpha = 0.0062(2)$. The g factor of the samples with $\lambda \leqslant 103$ nm was determined as $g = 2.11(1)$.

			D		ΔH_{pp}^{inh}		
λ (nm)	rms (nm)	δ (nm)	easy (T nm^2)	hard (T nm^2)	easy (mT)	hard (mT)	α hard
–	0.2	–	24(1)	24(1)	0.3	0.4	0.0062(2)
27	0.9	1.8	24(1)	21(1)	0.5	1.2	0.0063(2)
35	1.7	2.3	24(1)	21(1)	0.7	0.7	0.0062(2)
47	2.5	3.5	24(2)	26(1)	0.5	0.3	0.0065(2)
103	2.7	6	25(1)	24(1)	1.1	0.5	0.0063(2)
222	12.3	30	26(1)	25(2)	0.6	1.0	0.0075(3)
341	27.9	61	–	–	–	–	–
432	16.5	60	–	–	–	–	–

cross-section images of the two rippled samples with wavelength of 47 and 222 nm were recorded. In each of both images, four different layers are observable, as depicted in Figs. 3(c) and 3(d). At the bottom, the Si substrate is visible, which is followed by amorphous Si. In the case of $\lambda = 47$ nm, this layer has a thickness of 1–2 nm, which is barely visible and mainly originates from natural oxidation when transferring the substrate under ambient condition. In contrast, the $\lambda =$ 222 nm case shows an enlarged amorphous layer unevenly distributed with the surface corrugation. This is caused by strongly increased ion energies of 40 keV during sputtering, necessary to prepare high-wavelength ripples. Here, the ions penetrate the Si surface causing amorphization within the ion penetration depth, while shadowing effects of the corrugated surface, together with the tilted ion incidence angle, cause the asymmetric shape. Due to the amorphous substrate surface, the deposited layers of Py and Cr grow in a polycrystalline fashion. Finally, the TEM images end with a carbon layer deposited prior to the lamella cutting to protect the magnetic layers during FIB milling.

Both TEM images show a congruent layer growth, where no curvature dependent thickness variation can be observed. To visualize this parallelism between the layer's upper and lower interfaces, the lower one was marked by a dashed white line that was duplicated and parallelly shifted to the upper interface, perfectly reproducing it. Therefore, for both thicknesses, no significant thickness variation was observed excluding dipolar fields that would originate from varying layer thicknesses.

In Ref. 32, it was shown that rippled magnetic films, comparable to the one shown in Fig. 3(c), exhibit dipolar magnetic fields causing the magnetization to align partially with the surface corrugation.[42] However, the tilt away from the perfect alignment of a planar film is rather small. This also applies to the dipolar field strengths when being compared to the magnetization, which justifies the assumption of perturbation in this modulation limit. Nevertheless, the TEM image in Fig. 3(d) shows that film thickness and ripple amplitude are comparable to each other for a wavelength of $\lambda = 222$ nm. Additionally, the exchange length for Py is typically around

5 nm and thus well below the modulation length of the surface. Therefore a parallel alignment of the magnetization with the surface corrugation can be expected. To prove this assumption, micromagnetic simulations will be discussed in the following.

The sample geometry for the simulation was taken from Fig. 3(d) where the interface corrugation was extracted from the image and implemented in OOMMF using a polynomial ansatz. For simplicity, only one interface was approximated and the derived function shifted by the film's thickness $d = 30$ nm to model the magnetic film. The other parameters were set to $\mu_0 M_s = 1$T, $D = 24\ \mathrm{T\,nm^2}$, and $\lambda = 216$ nm, where the latter originates from the TEM picture and differs only slightly from the averaged value determined by AFM. The cell size of the simulation grid [using the coordinate system depicted in Fig. 3(d)] was set to $1 \times 5 \times 0.5\ \mathrm{nm^3}$, which is much below the exchange length and necessary to model the surface corrugation in order to minimize artifacts caused by step edges. The simulation volume was $216 \times 50 \times 100\ \mathrm{nm^3}$ with periodic boundary conditions along the x direction. In order to prevent y from being an easy axis the slice geometry—equivalent to the TEM geometry—was chosen, enabling investigation of the magnetization with and without external field along the direction of interest (x).

As expected, the magnetic moments align parallel with the surface modulation for vanishing external field and start to reorient along the field direction if an external field is present. This is exemplarily shown in Fig. 4(a), where a single slice along the y direction is presented for an external field of 0.5 mT along the x direction showing the magnetization alignment (arrows: x, color: z component). Red (blue) colors label positive (negative) values and green (orange) arrows mark positive (negative) orientations. Even for vanishing external field the magnetization alignment is not perfect with the surface, which in turn gives rise to stray fields. If the

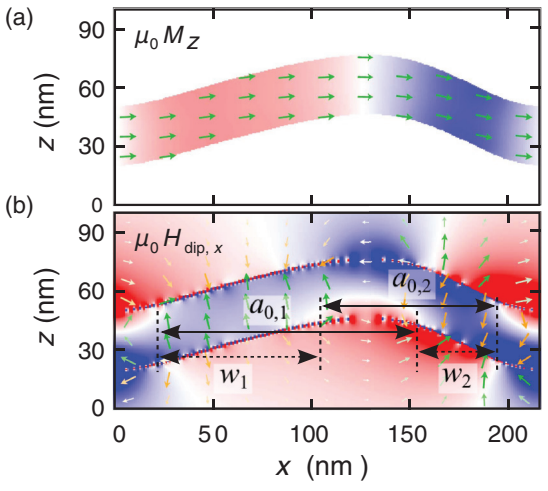

FIG. 4. (Color online) Micromagnetic simulations of the ripple profile extracted from Fig. 3(d) for an external field of $\mu_0 H = 0.5$ T. The color code shows the component of (a) the magnetization along z and (b) the stray field along x, where red (blue) colors denote positive (negative) values. Small arrows denote the in-plane orientation, where the color displays (a) the x and (b) the z component with green (orange) colors denoting positive (negative) values. The full range of the color scale is (a) ±251 and (b) ±38 mT, respectively.

field strength is increased, the magnetization starts to point towards the ripple slopes, which enhances the dipolar field strength by keeping the pole positions nearly unchanged. In Fig. 4(b), the dipolar field is depicted evolving from the magnetization configuration shown in Fig. 4(a). In comparison to the magnetization, these fields are much smaller. This in turn justifies the assumption that the magnetic film is perturbed by dipolar fields, where only a slight influence on the magnetization can be observed. Nevertheless, the shape of the dipolar field is quite different to the stripe case. This will have a strong influence on the magnon scattering property and is discussed in detail below.

The magnetic investigations were performed using VNA-FMR, which allows to excite the samples in a broad frequency range. To explore the in-plane anisotropy and linewidth contributions, two types of measurement geometries were used: (i) a $f(H)$ dependence at fixed angles of the external field, usually along the easy and hard anisotropy direction, and (ii) an in-plane angular dependence that changes the in-plane angle of the external magnetic field. For the planar case, the in-plane angular dependence (not shown) reveals a uniaxial magnetic anisotropy $K_{2||}/M_s$ below 1 mT, as it is known for Py thin films. Cubic anisotropy contributions are one order of magnitude smaller, which is due to the poly-crystalline sample structure. For the effective magnetization $\mu_0 M_{\mathrm{eff}} = \mu_0 M_s - 2K_{2\perp}/M_s = 1021$ mT was measured, which is close to $\mu_0 M_s$. This indicates that the out-of-plane anisotropy contribution $K_{2\perp}/M_s$ is negligible. From the $f(H)$ dependence, the g factor was determined resulting in $g = 2.11(1)$.

In Fig. 5, the measurements are depicted for a planar reference sample. The frequency-dependent resonance field shows, next to the FMR mode, a second branch that corresponds to a perpendicular standing spin wave[43] (PSSW) and allows to determine the exchange stiffness D, as $D = 24(1)\ \mathrm{T\,nm^2}$. Besides that, Fig. 5(b) shows the frequency dependence of the peak-to-peak linewidth of the FMR signal recorded along the easy axis of the sample. The linewidth of the PSSW mode equals the linewidth of the FMR mode and therefore is not shown. The linear increase indicates pure Gilbert damping, that can be modeled by

$$\Delta H_{\mathrm{pp}}^{\mathrm{G}} = \frac{2}{\sqrt{3}} \frac{\alpha}{\gamma} \omega \tag{6}$$

and is also obtained from Eq. (5) if the perturbation term Γ^{I} vanishes. Note that the factor $2/\sqrt{3}$ is used to convert between half-width half-maximum and peak-to-peak linewidth ΔH and ΔH_{pp}, respectively. To account for the case of a residual linewidth at zero frequency, a frequency independent contribution $\Delta H_{\mathrm{pp}}^{\mathrm{inh}}$ is added to the Gilbert damping term, which is also known as inhomogeneous line broadening. Applying Eq. (6) and the inhomogeneous broadening to the data gives a Gilbert damping of $\alpha = 0.0062(2)$ and an inhomogeneous line broadening of $\Delta H_{\mathrm{pp}}^{\mathrm{inh}} = 0.25$ mT for the easy axis. Along the hard axis, the same Gilbert damping behavior is observed, while the inhomogeneous broadening slightly increased to $\Delta H_{\mathrm{pp}}^{\mathrm{inh}} = 0.35$ mT. Hence the planar reference sample shows an isotropic in-plane linewidth, dominated by Gilbert-like relaxation mechanisms. A corresponding behavior was also observed for the in-plane angular dependence (not shown).

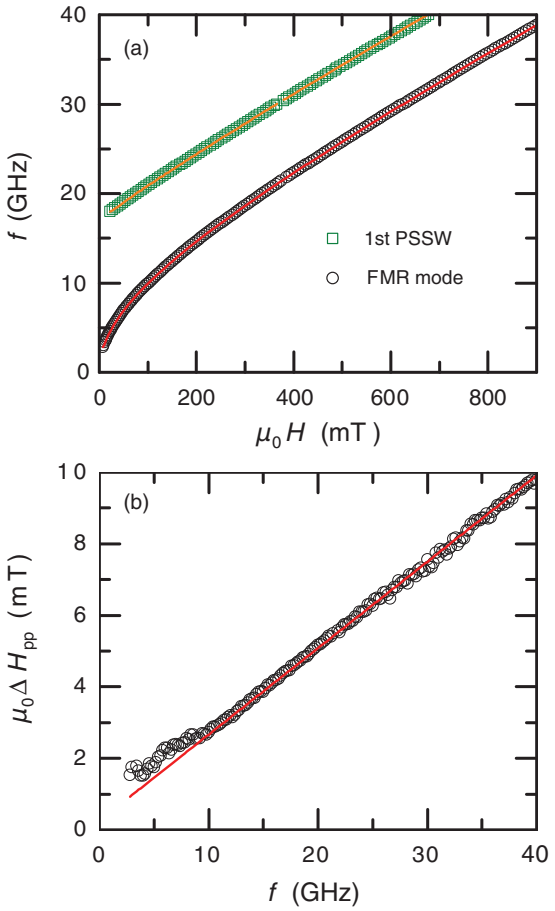

FIG. 5. (Color online) Planar reference sample of 30 nm Py. (a) Field dependence of the FMR mode (black circles) and the first PSSW (green squares). (b) The linewidth of the FMR mode. For clarity the linewidth of the PSSW is not shown as it is identical to the FMR mode's linewidth. The solid lines are fits to the data.

Now we turn to the rippled samples. From Fig. 2(a) it becomes clear that not all reciprocal periodicities $g_0 = 2\pi/a_0$ will trigger TMS scattering. A too small a_0 causes the reciprocal lattice number g_0 to be bigger than the k distance of the degenerate states. Therefore TMS will occur only at very high field/frequency values and thus out of the measurement range. Additionally, peaks at high frequencies are broadened due to intrinsic damping and will be hardly visible with respect to the latter. To estimate the lower modulation limit necessary to observe TMS within a 30 GHz measurement range, two basic assumptions can be made: (i) the defect periodicity equals the wavelength, so $a_0 = \lambda$ and (ii) the defect width is roughly half the wavelength $w = \lambda/2$, which is due to the asymmetry of the ripples, a very rough estimation that will be discussed in detail later. Using this parameter set, the perturbation theory predicts no changes in linewidth (within the given frequency range of up to 30 GHz) if the wavelength stays below $\lambda_{\mathrm{crit}} \approx 70$ nm. Hence, to determine the general impact of rippled surfaces onto magnetic properties, samples are investigated that have a wavelength around and below the limit. Like in the case of the planar reference, the samples discussed below exhibited a negligibly small fourfold anisotropy. However, the in-plane twofold contribution strongly increased, which has

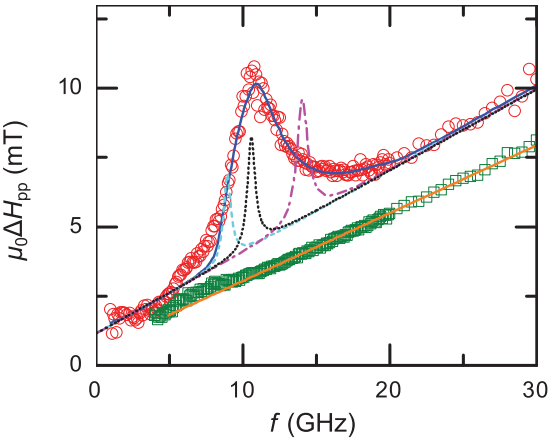

FIG. 6. (Color online) Frequency dependent linewidth measured parallel (green squares) and perpendicular to the ripple ridges (red circles) of $\lambda = 222$ nm. Solid lines are fits using the perturbation theory (blue) or Gilbert damping (orange), respectively. The cyan dashed line depicts the case of $a_{0,1} = 137$ nm, $w_1 = 62$ nm, and the magenta dashed dotted line $a_{0,2} = 88$ nm, $w_2 = 39$ nm. The black dotted line is the average case with $\bar{a}_0 = 112.5$ nm, $\bar{w} = 50.5$ nm.

its origin in the dipolar fields evolving if the magnetization is perpendicularly oriented to the ripple crests.[42] This behavior is discussed in detail in Ref. 32. Using $f(H)$ measurements the g factor was found to be isotropic for all samples up to $\lambda = 103$ nm. In addition, the first PSSW mode was observed again. From this, D was extracted. Along the easy axis, D equals the planar reference value, while measurements along the hard axis showed a slight decrease of $D = 21(1)\,\mathrm{T\,nm^2}$ for samples with $\lambda = 27$ nm and $\lambda = 35$ nm. Increasing the wavelength to $\lambda = 47$ nm yields the planar value instead. Since the determination of the exchange stiffness includes the in-plane UMA contribution, the deviation may originate from structural changes caused by the ripple morphology at small wavelengths. Furthermore, no changes in the intrinsic damping factor α were found within the experimental precision, being isotropic over the whole in-plane angular dependence. Most important, no influence of the frequency-dependent linewidth in form of peaks could be observed.

In contrast, increasing the ripple wavelength to $\lambda = 222$ nm has a strong impact on the linewidth behavior when the measurement is taken perpendicularly to the ripple ridges. The corresponding measurements are depicted in Fig. 6. While the linewidth parallel to the ripple ridges shows again pure Gilbert damping, the perpendicular orientation reveals a well pronounced peak. Surprisingly, for the frequency range considered here, only a single peak is observed, which, in addition, has a much broader distribution than an equivalent stripelike perturbed film (black dotted curve). The absence of higher-order peaks may have different reasons: (i) if the surface modulation is a sinusoidal function Eq. (4) provides just a rough estimation of a 1D modulated charge distribution if m is limited to $m = \pm 1$, and thus, only a single peak (corresponding to g_0) would result. (ii) The modulation periodicity is a multiple of the defect width and thus suppresses peaks or (iii) the interplay between defect periodicity/width and exchange stiffness simply shifts the peak out of the measurement range. The first two arguments can be ruled out immediately if the

spatial distribution of the dipolar field is considered. Hence, observing only a single peak within the measurement range can be attributed to the chosen geometry of the modulation. The final slope of the linewidth with f (red open circles) indicates that there should be a second peak at $f > 30$ GHz. Otherwise the slope of the red circles and the green squares should be equal.

To compare the model with the measurement, the parameters of the surface modulation need to be adapted to the perturbation model. With respect to magnetic properties, $\mu_0 M_s = 1$ T and $d = 30$ nm were used. Again, the first PSSW mode was used to determine the exchange stiffness to $D = 25(2)$ T nm^2 [$D = 26(1)$ T nm^2] along the hard (easy) axis, which is comparable to the $\lambda = 103$ nm case. However, note that the evaluation is based on the assumption of vanishing influences of TMS with respect to the resonance position. Since the g factor determination is very sensitive on the resonance position, the previously determined value of $g = 2.11$ was used. In contrast, D is most sensitive to the spacing between the FMR and PSSW mode. Due to the unknown influence of TMS also in this case the planar reference value of $D = 24$ T nm^2 was used. Furthermore, the defect periodicity ($a_0 = 216$ nm) is taken from the TEM images, whereas the defect width corresponds to the length on the ascending or descending ripple slope, as described in the next paragraph. Note that the choice between the two possibilities of the defect width has no influence on the result as long as both widths sum up to the defect periodicity.

However, using the parameters obtained in this way results in a first linewidth peak at a frequency of $f \approx 6.5$ GHz and is thus well below the experimentally observed peak position of $f = 10.7(3)$ GHz. Keeping anisotropy K_i, the spin wave propagation angle φ_k, and film thickness d fixed, mainly two parameters determine the peak position, namely the defect periodicity a_0 and the exchange stiffness D. Since the latter has to be changed by a factor of two to match the experimental observation—which is not seen in the recorded modes—the initial assumption of equal ripple wavelength and defect periodicity has to be reconsidered.

To do so, the dipolar fields created by the rippled morphology will be compared with the stripelike defect structure assumed by the theory. Based on Eq. (4) Landeros and Mills derived an expression for the in-plane dipolar stray field component generated by a surface stripe pattern as it is depicted in Fig. 1. The corresponding field pattern is shown in Fig. 7 for a 30 nm Py film with a defect height of $h = 3$ nm, periodicity of $a_0 = 250$ nm, and defect width $w = 115$ nm. Note that only the stray field component inside the Py film is depicted neglecting the defect structure. The underlying periodicities are denoted by arrows highlighting a_0 and w. As it can be seen from the image, the stray field changes once its strength inside the film over the defect period in a steplike manner and is thus divided into two parts with nearly constant field strengths. Thereby, the stray field below the stripe defect nearly vanishes, while it has a much higher value next to the stripe with a steplike transition region.

This in turn is not the case for the rippled geometry, where the field modulation changes continuously with the surface corrugation as it is shown in Fig. 4(b). More important, due to the rising and falling slopes, the film exhibits minima and

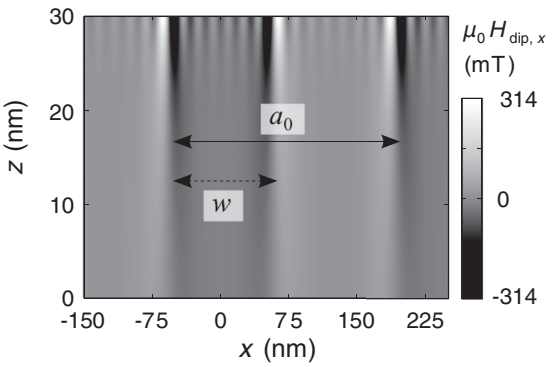

FIG. 7. Plot of the dipolar stray field assumed in the perturbation theory caused by stripe defects of $a_0 = 250$ nm, $w = 115$ nm, and $h = 3$ nm. Only the configuration inside a 30 nm thick Py ($\mu_0 M_s = 1$ T, $D = 24$ T nm^2, external field of 0.1 T along the x axis) film is shown.

maxima at which the dipolar fields reverse the sign across the film's thickness. Since the magnetization is aligned in the plane and due to two opposing curvatures across a single wavelength not only a single periodicity is observed but multiple ones. Exemplarily, two periodicities and corresponding defect widths are highlighted in Fig. 4(b). From the image, the values $a_{0,1} = 137$ nm, $w_1 = 62$ nm, and $a_{0,2} = 88$ nm, $w_2 = 39$ nm were taken. The resulting linewidths are calculated for both cases where the obtained frequency dependencies are plotted in Fig. 6 by a cyan dashed line and a magenta dashed dotted line, respectively. For the defect height, an arbitrary value of $h = 1$ nm was chosen to scale the height of the linewidth peaks to the measurement. Both resulting peaks are covered by the measured peak with respect to its frequency position. Since the ripple morphology creates a continuous transition in the stray field not a single parameter set is obtained but a continuous range of periodicities and corresponding widths. This continuous range superimposes multiple peaks, which sum up in the measurement and results in a broadened peak distribution. Simply averaging the two given periodicities—basically the limiting cases—results in $\bar{a}_0 = 112.5$ nm and $\bar{w} = 50.5$ nm, which is plotted in Fig. 6 by a black dotted line reproducing the peak's center. Note also that $\bar{a}_0$ almost equals half the wavelength of $\lambda = 222$ nm, which is obvious since the two extrema of the surface corrugation have a mean distance of $\lambda/2$. In order to approximate the measured linewidth peak by a model of continuously superimposed peaks a series of 200 model curves was averaged changing the defect periodicity a_0 linearly between 72 and 139 nm and the defect width between 39 and 62 nm. The slight deviation to the previously determined a_0 range simply results from uncertainties in the graphical determination of a_0 from the cross-sectional TEM image, where additionally only a single wave was evaluated neglecting a variation in the wavelength as it is suggested by the AFM images shown in Fig. 3. In contrast, w does not influence the frequency position of the first order peaks and, thus, cannot be approximated by the fit.

For the defect height h, a linear dependence was assumed starting at 1.2 nm at the lower limit of a_0 increasing to 3.5 nm when reaching the center of the defect range and finally decreasing again to 1.2 nm until the upper limit of

a_0 is reached. This assumption is justified by Fig. 4(b) since the strongest dipolar fields are roughly separated by half the wavelength in distance, while shorter/longer periods have smaller dipolar fields. In this way, the morphology of a single ripple wave is approximated by stripe defects with respect to the dipolar fields. Note that inhomogeneities caused by the varying ripple quality are neglected. The resulting curve is depicted in Fig. 6 by the blue solid line, perfectly reproducing the data. It also reproduces the asymmetry of the peak's slopes, which are caused by the increasing linewidth of single peaks occurring with increasing microwave frequency (cf. cyan dashed and magenta dashed dotted curves). Note that due to averaging the resulting peak height appears much smaller than a single linewidth peak calculated with $h = 3.5$ nm would look like. As mentioned earlier, perturbations cause a shift and splitting of the measured resonance. Although this has a remarkable influence when calculating the film's response for a single a_0, w set the averaging over a whole range causes a line shape where the determination of a single resonance position and width is possible. However, this means that the observed line broadening results from averaging resonances and, thus, is apparent. An increase in damping would only be present if the $k \neq 0$ modes—excited by TMS—exhibit an increased damping with respect to the $k = 0$ mode. Finally, the Gilbert damping $\alpha = 0.0062(2)$ derived from the measurement equals the value for the reference sample if measured parallel to the ripple ridges and increases to $\alpha = 0.0075(3)$ for perpendicular alignment.

The peak position as well as its magnitude is influenced by the ripple wavelength set during sample preparation and by the external field direction with respect to the ripple ridges during measurement. Both cases are depicted in Fig. 8, where panel (a) shows the frequency dependent linewidth for different angles with respect to the ripples. Here, φ_H measures the angle between external field and the direction perpendicular to the ripple ridges of the $\lambda = 222$ nm sample. By increasing φ_H the linewidth peak slightly shifts up in frequency by simultaneously decreasing in magnitude. The latter is understood in the framework of the dipolar field strength that is responsible for triggering TMS. By rotating the magnetic fields towards the easy axis (parallel to ripple ridges) the dipoles become weaker in strength and finally vanish if the easy axis alignment is reached (black diamonds). To include this into the perturbation theory, as it is pointed out in Ref. 30, Γ^I needs to be scaled by $\cos^4 \varphi_H$. It might be tempting to discuss this within context of the critical angle, where TMS shuts off if φ_k exceeds a critical value, thus suppressing the mode degeneration.[18,33] However, the estimated critical angle of $\varphi_c = 20^\circ$ does not explain the entire angular dependence (not shown), since the multiple periodicities and the imperfect ripple structure may further broaden the critical angle, as it occurs with the linewidth peak in Fig. 6. Here, a superposition of different stripes was considered to fit the data. Although the experimental data do not follow exactly the critical angle criteria, the individual stripes indeed follow this criteria, having a narrow angular dependence with the corresponding shut-off of TMS if φ_k exceeds the critical angle.

The increasing peak position can be understood considering the following. (i) The resonance condition (1) includes the spin wave propagation angle φ_k entering the stiffness field $H_{||}$ in

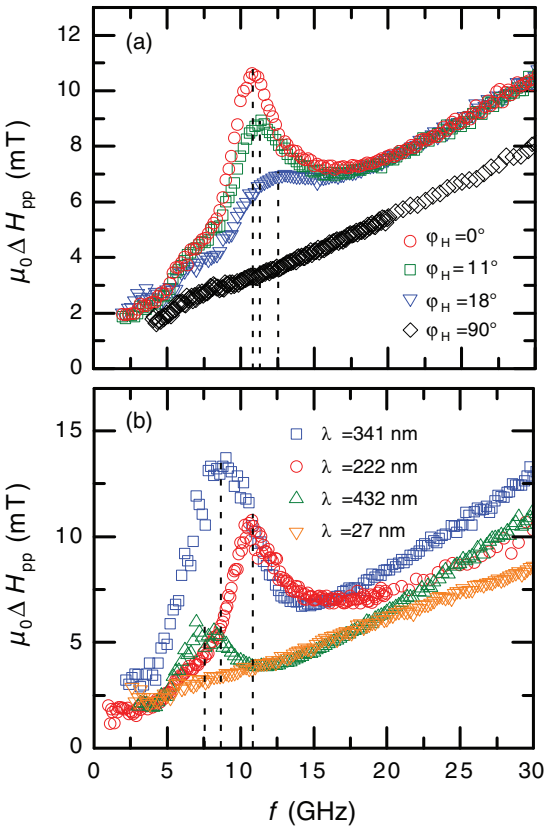

FIG. 8. (Color online) Linewidth peak in dependence of (a) the external field orientation φ_H for $\lambda = 222$ nm and (b) the ripple wavelength λ at $\varphi_H = 0^\circ$. Dashed lines mark the peak maxima.

Eq. (2). The perturbation direction triggering the spin waves is set by the ripple ridges. Thus, under the assumption that $\vec{k}$ is perpendicular to the ridges, φ_k increases if the magnetization is turned away from the perpendicular alignment by changing φ_H. (ii) When the $\vec{H}$ component along the hard magnetization axis is reduced this may influence the dipolar stray field distribution. This in turn alters the scattering periodicity and thus the linewidth peak position, but no significant changes in the stray field periodicity are observed in Fig. 4. In addition, this effect leads to a reduction in scattering strength and hence the amplitude of the linewidth peak is reduced.

For Fig. 8(b), the frequency dependent linewidth was recorded perpendicularly to the ripple ridges and plotted as a function of ripple wavelength. For comparison, the reference case of $\lambda = 27$ nm having no peak is shown. The remaining wavelengths show a decrease in peak position with increasing ripple wavelength. Due to increasing λ the average periodicity $\bar{a}_0$ increases, which thus leads to a decrease in the reciprocal lattice vector g_0. Therefore the scattering condition is fulfilled at lower fields corresponding to lower microwave frequencies.

From the peak positions of the $\lambda = 341$ nm case and $\lambda = 432$ nm the averaged periodicity was determined to be $\bar{a}_0 = 146(14)$ and $182(30)$ nm. Within the given error, these corresponds to the surface modulations set by the ripples. The height of the peak is influenced by the ratio between defect width and periodicity [see Fig. 2(b)]. This ratio changes with the ripple wavelength.

Another interesting feature is observed well above the linewidth peaks in Fig. 8(b). The slope of the data of the 341 and 432 nm sample remarkably differ from the other two samples. The reason might be the evolution of a broad second peak. Hence, Gilbert damping is not the only linewidth contribution in this range. This in turn could also explain the higher α value seen in Fig. 6 for perpendicular alignment.

Proven by TEM cross-section images [see Fig. 3(d)], ripples obey no perfect sinusoidal modulation and hence those higher-order linewidth peaks ($|m| > 1$) should exist. Smaller defect periodicities, e.g., caused by nonperfect ripples, will cause even higher frequencies. Calculations show that the higher order peaks are broader. Hence they might blend into the linear Gilbert background, thus increasing the slope. Nevertheless, in the calculation of the $\lambda = 222$ nm case, no further peaks at higher frequencies exist. This suggests that other (smaller) defect periodicities may be present in the samples that are neglected in the model. Such contributions may come from the variation of the ripple quality, whereas the model assumes a perfect ripple periodicity of the simulated single wave shown in Fig. 4.

V. SUMMARY

In this work, we investigated the influence of periodically modulated substrates on 30 nm thin Py films with respect to magnetic relaxation properties. From investigations presented earlier, it is known that rippled substrates introduce an UMA that in turn is caused by periodic dipolar stray fields generated by the modulated surface. These fields were used to extrinsically modify the relaxation mechanisms by introducing two-magnon scattering. In contrast to intrinsic Gilbert damping, TMS is strongly direction dependent and correlated to the surface morphology. Hence the frequency-dependent linewidth is enhanced when measuring perpendicularly to the ripple ridges and reduces to the Gilbert contribution for parallel alignment. In the first case, a peak evolves for sufficiently high wavelengths, whose frequency position is determined by the periodicity of the surface modulation. This can be understood in the framework of the perturbation theory presented by Landeros and Mills as a superposition of different scattering periodicities causing an apparent increase in the measured linewidth. Additionally, influences on the in-plane angle-dependent linewidth behavior are found. The symmetry in linewidth is caused by the symmetry of the substrate's surface modulation. Therefore using rippled substrates provides a fast and easy method to extrinsically tailor magnetic relaxation by simply changing the magnetic *field* direction or the excitation *frequency* of the microwave field. Especially the first alters the linewidth by up to 500% in magnitude if the magnetization direction is switched between easy and hard axis alignment.

ACKNOWLEDGMENTS

We thank I. Winkler and F. Ludewig for ripple preparation. This work has been supported by the Deutsche Forschungsgemeinschaft (Grant No. FA 314/6-1), FONDECYT 1120618, CONICYT and the program "Financiamiento Basal para Centros Científicos y Tecnológicos de Excelencia" CEDENNA FB0807.

*Corresponding author: m.koerner@hzdr.de

[1] I. Barsukov, R. Meckenstock, J. Lindner, M. Möller, C. Hassel, O. Posth, M. Farle, and H. Wende, IEEE Trans. Magn. **46**, 2252 (2010).
[2] J. Fassbender and J. McCord, Appl. Phys. Lett. **88**, 252501 (2006).
[3] I. Žutić, J. Fabian, and S. Das Sarma, Rev. Mod. Phys. **76**, 323 (2004).
[4] A. Brataas, A. D. Kent, and H. Ohno, Nat. Mater. **11**, 372 (2012).
[5] G. S. D. Beach, M. Tsoi, and J. L. Erskine, J. Magn. Magn. Mater. **320**, 1272 (2008).
[6] S. A. Wolf, D. D. Awschalom, R. A. Buhrman, J. M. Daughton, S. von Molnár, M. L. Roukes, A. Y. Chtchelkanova, and D. M. Treger, Science **294**, 1488 (2001).
[7] *Ultrathin Magnetic Structures III: Fundamentals of Nanomagnetism*, edited by J. A. C. Bland and B. Heinrich (Springer-Verlag, Berlin Heidelberg, 2005).
[8] T. L. Gilbert, IEEE Trans. Magn. **40**, 3443 (2004).
[9] B. Heinrich, R. Urban, and G. Woltersdorf, IEEE Trans. Magn. **38**, 2496 (2002).
[10] D. L. Mills and S. M. Rezende, in *Spin Dynamics in Confined Magnetic Structures II*, edited by B. Hillebrands and K. Ounadjela (Springer-Verlag, Berlin Heidelberg, 2003).
[11] Z. Celinski and B. Heinrich, J. Appl. Phys. **70**, 5935 (1991).
[12] V. Kamberský, Czech. J. Phys. B **26**, 1366 (1976).
[13] J. Seib, D. Steiauf, and M. Fähnle, Phys. Rev. B **79**, 092418 (2009).
[14] G. Woltersdorf and B. Heinrich, Phys. Rev. B **69**, 184417 (2004).
[15] R. C. LeCraw, E. G. Spencer, and C. S. Porter, Phys. Rev. **110**, 1311 (1958).
[16] M. Sparks, R. Loudon, and C. Kittel, Phys. Rev. **122**, 791 (1961).
[17] C. E. Patton, J. Appl. Phys. **39**, 3060 (1968).
[18] R. Arias and D. L. Mills, Phys. Rev. B **60**, 7395 (1999).
[19] R. D. McMichael, D. J. Twisselmann, and A. Kunz, Phys. Rev. Lett. **90**, 227601 (2003).
[20] R. D. McMichael and P. Krivosik, IEEE Trans. Magn. **40**, 2 (2004).
[21] A. Azevedo, A. B. Oliveira, F. M. de Aguiar, and S. M. Rezende, Phys. Rev. B **62**, 5331 (2000).
[22] J. Lindner, K. Lenz, E. Kosubek, K. Baberschke, D. Spoddig, R. Meckenstock, J. Pelzl, Z. Frait, and D. L. Mills, Phys. Rev. B **68**, 060102 (2003).
[23] K. Lenz, H. Wende, W. Kuch, K. Baberschke, K. Nagy, and A. Janossy, Phys. Rev. B **73**, 144424 (2006).
[24] Kh. Zakeri, J. Lindner, I. Barsukov, R. Meckenstock, M. Farle, U. von Horsten, H. Wende, W. Keune, J. Rocker, S. S. Kalarickal, K. Lenz, W. Kuch, K. Baberschke, and Z. Frait, Phys. Rev. B **76**, 104416 (2007) and Erratum.
[25] S. Schäfer, N. Pachauri, C. K. A. Mewes, T. Mewes, C. Kaiser, Q. Leng, and M. Pakala, Appl. Phys. Lett. **100**, 032402 (2012).
[26] L. Lu, J. Young, M. Wu, C. Mathieu, M. Hadley, P. Krivosik, and N. Mo, Appl. Phys. Lett. **100**, 022403 (2012).

[27]R. D. McMichael, D. J. Twisselmann, J. E. Bonevich, A. P. Chen, W. F. Egelhoff, and S. E. Russek, J. Appl. Phys. **91**, 8647 (2002).
[28]D. J. Twisselmann and R. D. McMichael, J. Appl. Phys. **93**, 6903 (2003).
[29]I. Barsukov, F. M. Römer, R. Meckenstock, K. Lenz, J. Lindner, S. Hemkento Krax, A. Banholzer, M. Körner, J. Grebing, J. Fassbender, and M. Farle, Phys. Rev. B **84**, 140410(R) (2011).
[30]P. Landeros and D. L. Mills, Phys. Rev. B **85**, 054424 (2012).
[31]M. O. Liedke, M. Körner, K. Lenz, F. Grossmann, S. Facsko, and J. Fassbender, Appl. Phys. Lett. **100**, 242405 (2012).
[32]M. O. Liedke, M. Körner, K. Lenz, M. Fritzsche, M. Ranjan, A. Keller, E. Čižmár, S. A. Zvyagin, S. Facsko, K. Potzger, J. Lindner, and J. Fassbender, Phys Rev. B **87**, 024424 (2013).
[33]P. Landeros, R. E. Arias, and D. L. Mills, Phys. Rev. B **77**, 214405 (2008).
[34]J. Lindner, I. Barsukov, C. Raeder, C. Hassel, O. Posth, R. Meckenstock, P. Landeros, and D. L. Mills, Phys. Rev. B **80**, 224421 (2009).
[35]I. Barsukov, P. Landeros, R. Meckenstock, J. Lindner, D. Spoddig, Zi-An Li, B. Krumme, H. Wende, D. L. Mills, and M. Farle, Phys. Rev. B **85**, 014420 (2012).
[36]J. Fassbender, T. Strache, M. O. Liedke, D. Markó, S. Wintz, K. Lenz, A. Keller, S. Facsko, I. Mönch, and J. McCord, New J. Phys. **11**, 125002 (2009).
[37]A. Keller, S. Roßbach, S. Facsko, and W. Möller, Nanotechnol. **19**, 135303 (2008).
[38]I. Horcas, R. Fernandez, J. M. Gomez-Rodriguez, J. Colchero, J. Gomez-Herrero, and A. M. Baro, Rev. Sci. Instrum. **78**, 013705 (2007).
[39]http://gwyddion.net/
[40]http://math.nist.gov/oommf/
[41]A. Keller and S. Facsko, Materials **3**, 4811 (2010).
[42]R. Arias and D. L. Mills, Phys. Rev. B **59**, 11871 (1999).
[43]S. O. Demokritov and B. Hillebrands, in *Spin Dynamics in Confined Magnetic Structures I*, edited by B. Hillebrands and K. Ounadjela (Springer-Verlag, Berlin Heidelberg, 2002).